Downstream Evolution of Longitudinal Embedded Vortices with Helical Structure

Velte, Clara Marika; Okulov, Valery; Hansen, Martin Otto Laver

Published in:
Proceedings of the 8th International Symposium on Particle Image Velocimetry

Publication date:
2009

Document Version
Peer reviewed version

8TH INTERNATIONAL SYMPOSIUM ON PARTICLE IMAGE VELOCIMETRY - PIV09
Melbourne, Victoria, Australia, August 25-28, 2009

Downstream Evolution of Longitudinal Embedded Vortices with Helical Structure

C. M. Velte[1], V. L. Okulov and M. O. L. Hansen

[1]Department of Mechanical Engineering, Technical University of Denmark, Kgs. Lyngby, DK-2800, Denmark
cmve@win.dtu.dk

ABSTRACT

In the present work the downstream development of device induced vortices with helical symmetry embedded in wall bounded flow on a bump is studied with the aid of Stereoscopic Particle Image Velocimetry (SPIV). The downstream evolution of characteristic parameters of helical vortices is studied, displaying a linear variation of the helical parameters up to the trailing edge of the bump where the vortex experiences an abrupt transition in structure.

1. INTRODUCTION

Streamwise vortices embedded in turbulent boundary layers is a common phenomenon and is seen e.g. in the treatment of free organized structures (see e.g. [1] and references therein), Görtler vortices in boundary layers over walls of streamwise concave curvature [2], corner vortices with an axial velocity component, vortex rings near walls and as horseshoe vortices folding around objects attached to a wall [1]. Often longitudinal vortices are generated with passive devices called vortex generators. A vortex generator is similar to a wing with a small aspect ratio mounted normally to a surface with an angle of incidence to the oncoming flow. It is designed to overturn the boundary layer flow via large scale motions, thereby redistributing the streamwise momentum in the boundary layer which aids in preventing separation. Vortex generators were formally introduced by H. D. Taylor [3] as an aid in suppressing separation in diffusers.

Being able to control/optimize parameters such as the strength and size of the longitudinal vortices to the existing flow setting is highly desired and it is therefore of interest to develop theories and models which can predict and describe these. Some models have been proposed in order to describe the flow, both theoretically (see e.g. [4]) as well as computationally (see e.g. [5,6]). The non-uniform axial component is often obtained by introducing a Gaussian distributed streamwise force component. However, this was so far merely introduced and never motivated more than on a purely empirical basis to compensate for the momentum deficit in the wake of the device.

The main objective of this work is the experimental investigation of the downstream development of device-generated vortices to define and optimize helical vortex structures in wall-bounded flow and to create a three-dimensional model which more correctly can describe the vortex flow. Previously, a lot of experimental work was done describing embedded vortices in boundary layer flows using single point measurement techniques (see e.g. [7,8]). However, the development of Stereoscopic Particle Image Velocimetry allows non-intrusive instantaneous 3C measurement realizations of the flow in a plane and is the predominating measurement technique for these investigations today (see e.g. [9,10]). Previous investigations have shown that vortices generated by rectangular vanes in wall bounded flow have a helical structure [11]. Further, a 2D model was constructed for the dominating primary vortex, showing good concurrence with the measurement data. The axial and azimuthal vorticity components are coupled according to the definition for helical symmetry of vorticity fields;

$$\begin{cases} \omega_r = 0 & (1a) \\ \omega_\theta/\omega_z = r/l & (1b) \\ \omega_z = \dfrac{\Gamma}{\pi\varepsilon^2}\exp(-r^2/\varepsilon^2) & (1c) \end{cases}$$

where l represents the helical pitch, see figure 1(b). The corresponding velocity formulation (2) can be found by integrating equation (1b), the convection velocity u_0 being the integration constant.

$$u_z = u_0 - \frac{r}{l}u_\theta \qquad (2)$$

Even though the vortex generators operated in a turbulent boundary layer, yielding relatively large perturbations, the vortices were observed to be stable in the experiments. In addition, this linear relation allows for averaging also in the azimuthal direction, hence one can average over the variations throughout the azimuthal coordinate and obtain helical symmetry in that respect.

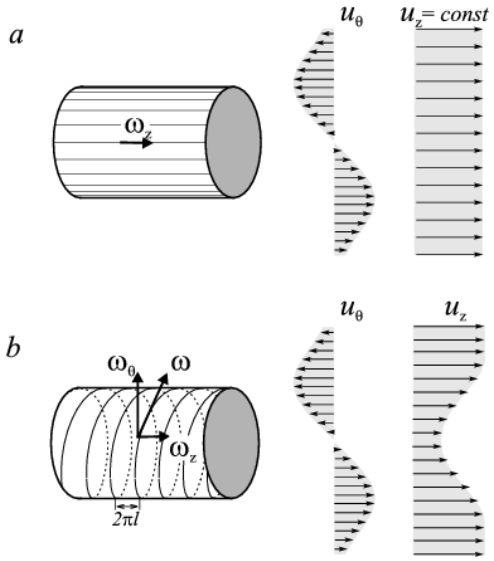

Figure 1. Sketch of vorticity field and induced velocity profile by Lamb-Oseen vortex with rectilinear vortex lines (a) and Batchelor vortex with helical structure of the vortex lines (b).

In the current study, measurements have been conducted in a low Reynolds number (free stream velocity U_∞=1.0 ms^{-1}) wall bounded flow on a cylindrical sector (bump) downstream of a vortex generator cascade, see figure 2, in order to study the flow processes generated by the devices. For a single vortex generator, a primary vortex is formed along with a weaker secondary one, perturbing the main vortex [11,12]. Mounting the generators in a cascade in a fashion producing counter-rotating primary vortices that are spaced densely enough results in cancelation of the secondary vortices. Hence, the net effect of each actuator is a monopole, see figure 3. A turbulent boundary layer profile was considered suitable due to a fuller velocity profile. This also makes the results more applicable to flows at more realistic Reynolds numbers. Turbulence was generated using an inlet grid to yield a high enough turbulence intensity to obtain a turbulent boundary layer profile. Results show that the vortex generators give rise to longitudinal vortices that possess helical symmetry. The helical parameters vary linearly across the bump chord up to the trailing edge of the bump where the vortex experiences an abrupt transition to a different state, obtaining a new structure.

2. EXPERIMENTAL METHOD

Consider the experimental setup in figure 2. The measurements were carried out in a closed-circuit wind tunnel with an 8:1 contraction ratio and a test section of cross-sectional area 300×600 mm with length 2 m. A circular sector (bump) spanning the width of the test section was placed on the test section wall with its leading edge 600 mm downstream of the inlet grid. The sector had a radius of 390 mm, a span of 600 mm, a width of 300 mm and a height of 30 mm. The test section had optical access through the top and bottom walls as well as through the sidewall opposite to the wall with the attached vortex generator. The coordinate system is defined at the measurement volume in figure 2. z is the axial flow direction, y is the wall-normal direction and x is the spanwise direction.

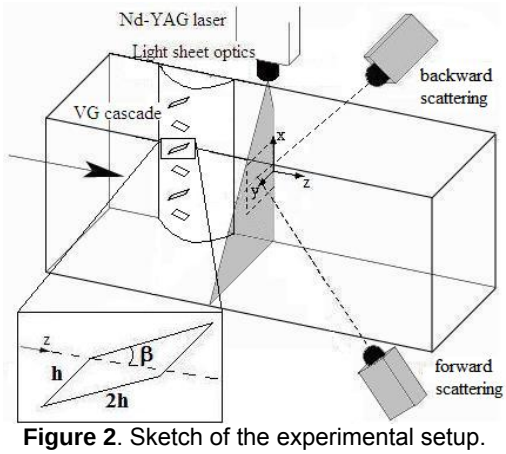

Figure 2. Sketch of the experimental setup.

The experiments were conducted at a free stream velocity of U_∞=1.0 ms^{-1}. The wind tunnel speed was obtained by measuring the pressure drop across an orifice plate. The turbulence intensity at the inlet has from LDA measurements been found to be 13%. The boundary layer thickness at the position of the vortex generator has been estimated from LDA measurements to be approximately δ_{VG}=25 mm. Rectangular actuators were chosen for the study since they provide a more symmetric vorticity distribution across the azimuthal direction in a cylindrical coordinate system centred at the vortex centre, as opposed to triangular vanes which generate a more skewed vorticity distribution. The vanes were places in a cascade along the span of the bump (β=18º, see [10] for exact configuration), in a fashion inducing counter rotating vortices, with the trailing edges at the bump centre. The vortex generator height was chosen based on the structure of the boundary layer. In this case, the low Reynolds number boundary layer was tripped by a grid of mesh size M=39 mm situated at the inlet. The turbulent boundary layer was chosen for its shape, having larger gradients close to the wall, yielding a more uniform velocity profile in the outer part of the boundary layer. The actuators were chosen as to produce vortices that mainly reside in this more uniform part of the boundary layer. As it facilitates the study of the vortices, it is also more similar to most applications.

PIV measurements involving reflecting surfaces such as walls etc. can often be cumbersome since the reflections can damage the camera CCD chip (or corresponding) and therefore only very low laser intensities can be used if at all. This will affect the signal (particle scattering), yielding a lower signal-to-noise ratio. Further, the reflections might appear in the areas of most interest, corrupting the signal and making it harder to distinguish the particle scattering. In order to tackle these problems, which in the current case comprises reflections from the test section and bump walls and actuators, a mixture of a fluorescent dye (Rhodamine 6G) and mat varnish was applied to these surfaces. The dye absorbs the laser light and re-emits at a shifted wavelength. The cameras were equipped with filters passing only light of wavelengths close to that of the laser. This method aided in reducing the unwanted reflections substantially, facilitating measurements close to the wall and the actuators. This made it possible to perform measurements as close as a couple of millimetres behind the actuators as compared to several centimetres before applying the dye.

Measurements have been conducted in spanwise planes (xy-plane) in a range of streamwise positions z, providing information about the downstream evolution of the longitudinal vortices. The stereoscopic PIV equipment was mounted on a rigid stand and included a double cavity NewWave Solo 120XT Nd-YAG laser (wavelength 532 nm), capable of delivering light pulses of 120 mJ. The pulse width, i.e. the duration of each illumination pulse, was 10 ns. The light sheet thickness at the measurement position was 2 mm and was created using a combination of a spherical convex and a cylindrical concave lens. The equipment also included two Dantec Dynamics HiSense MkII cameras (1344×1024 pixels) equipped with 60 mm lenses and filters designed to only pass light with wavelengths close to that of the laser light. Both cameras were mounted on Scheimpflug angle adjustable mountings. The seeding, consisting of DEHS droplets with a diameter of 2-3 μm, was added to the flow downstream of the test section in the closed-circuit wind tunnel in order to yield a homogeneous distribution of the particles before they enter the test section. The laser was placed above the test section, illuminating a plane normal to the test section walls, see figure 2. One camera was placed in the forward scattering direction and the other one in the backward scattering one. This configuration was chosen due to the obstruction of the view of one camera caused by the bump and actuators if both cameras were placed in the forward scattering direction. The angle of each respective camera to the laser sheet was 45º. The f-numbers of the cameras were set to between 8 and 16 (forward scattering) and 4 and 5.6 (backward scattering), depending on the relative light budget of the particle scattering and reflections. The SPIV setup was rigidly mounted on a traverse which could translate the setup

along the test section in the streamwise direction. In this manner, the calibration needed to be performed only once. A calibration target was aligned with the laser sheet. This target had a well defined pattern, which could be registered by the two cameras to obtain the geometrical information required for reconstructing the velocity vectors received from each camera to obtain a full description of all three velocity components in the plane. Calibration images were recorded with both cameras at five well defined streamwise positions throughout the depth of the laser sheet in order to capture the out-of-plane component in the reconstructed coordinate system of the measurement plane under consideration. A linear transform was applied to these images for each camera respectively to perform the reconstruction. This procedure was executed both previous to and after the conduction of the measurements to ensure that no drift had occurred. The images were processed using Dantec DynamicStudio software version 2.0. Adaptive correlation was applied using refinement with an interrogation area size of 32×32 pixels. Local median validation was used in the immediate vicinity of each interrogation area to remove spurious vectors between each refinement step. The overlap between interrogation areas was 50%. For each measurement position, 500 realizations were acquired. The disparity due to misalignment between the centre of the light sheet and the calibration target found in these investigations, typically around 0.05 pixels, were always smaller than the optimal measurement accuracy of the PIV system (0.1 pixels). The recording of image maps was done with an acquisition rate of 1.0 Hz, ensuring statistically independent realizations based on the convection velocity U_∞=1.0 ms^{-1} and the test section d=0.6 m, yielding a time scale of $t=d/U_\infty$=0.6 s. The velocity vector maps contain 73 by 61 vectors. The linear dimensions of the interrogation areas (x,y)=(1.55,1.04) mm can be compared to the Taylor microscale and the Kolmogorov length scale estimated to $\lambda_f \approx$ 9 mm and $\eta \approx$ 0.5 mm from Laser Doppler Anemometry (LDA) measurements [13].

3. RESULTS

As an overview of the development of the vortices, figure 3 displays the longitudinal velocity field obtained for some of the measurement planes in their approximate positions of acquisition along the bump and wind tunnel test section wall. The wind tunnel velocity direction is from the lower left corner to the upper right one.

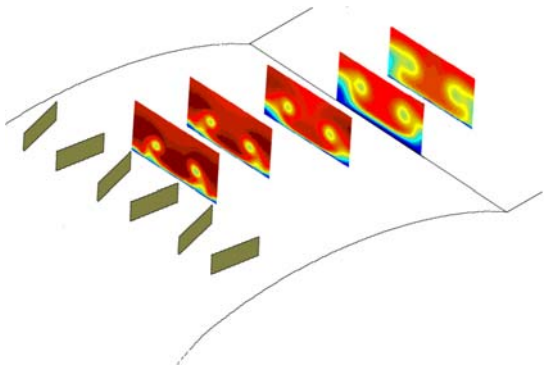

Figure 3. Sketch of bump and vortex generator cascade with longitudinal velocity component displayed by contour plots in some measurement planes placed approximately in their positions of acquisition. The velocity direction is from the lower left corner to the upper right one.

Figures 4(a-d) show the helical parameters of one of the measured vortices as a function of the downstream distance to the actuator cascade. The quantities are non-dimensionalized by the vortex generator height h and free stream velocity U_∞. ε and Γ were obtained from the expression for the vorticity distribution (1c). The convection velocity u_0, being the axial velocity at the centre of the vortex core, was obtained directly from the measurement data. The helical pitch was obtained in two different ways; by minimizing the residual of equation (2) in a least squares sense and through the swirl number S,

$$l = -F_{mm}/(F_m - u_0 G) \qquad (3)$$

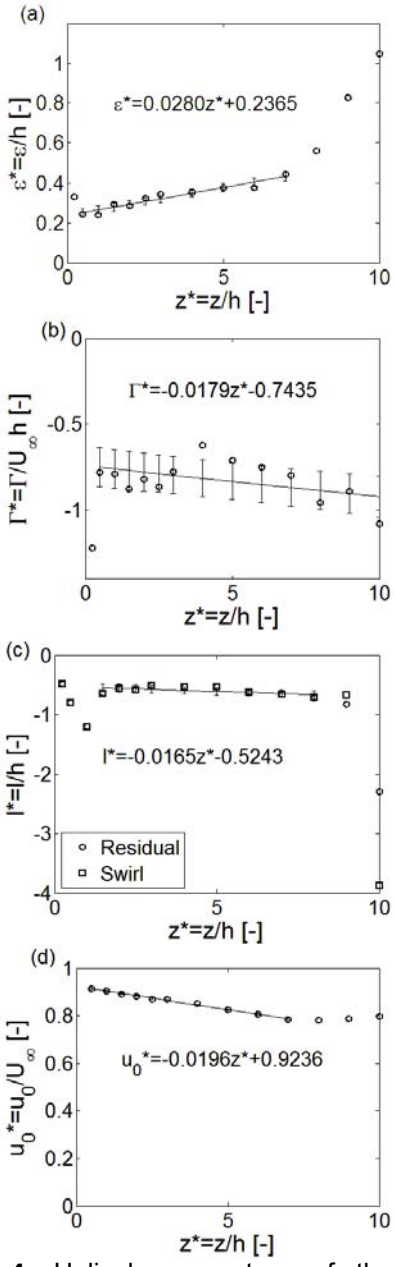

Figure 4. Helical parameters of the actuator induced vortex. The parameters have been non-dimensionalized by the vortex generator height h and free stream velocity U_∞ respectively. The parameters presented in each subfigure are the (a) vortex core radius, (b) estimate of the circulation, (c) helical pitch and (d) vortex convection velocity.

where F_{mm} and F_m are the angular and axial momentum flux in the axial direction, respectively. G is the flow rate, ρ is the fluid density and Σ is the cross-section area.

The circulation has a high variability, most probably as a result of inadequacy in the method of estimating the quantity. From the other parameters it is apparent that the vortex develops through 3 stages throughout the span of the measurements; Initially, the vortex is formed from the generated vortex sheet within a distance of approximately one vortex generator height. The vortex then reaches a stable region where the helical parameters vary linearly in the downstream direction approximately up to the position of the bump trailing edge (z*=6). This is seen by fitting the data by a linear approximation in a least squares sense and applying corresponding error bars. At the trailing edge of the bump, where the geometry experiences a sudden change, the pressure gradient will change accordingly, triggering an abrupt transition to another stage of the vortex to a helical symmetry with a different set of helical parameters, which begin to digress from the previous trend. The convection velocity ceases to decrease with downstream distance, while the vortex core radius grows more rapidly, partly due to the lower convection velocity. The increasing growth of the vortex core can also be seen in the downstream development of the vortices depicted in figure 3. The behaviour of the helical pitch above z*=6, which increases rapidly as one moves downstream, provides even further support for the hypothesis that the vortex has abruptly transferred to a new state.

The possibility of transition of a helical vortex to a different state without changing the sign of the helical pitch was predicted theoretically and supported by computations by Martemianov and Okulov [14]. This was shown by solving the energy equations and comparing the solutions obtained when the integral parameters (flow rate, circulation, axial flux of angular and axial momentum) were conserved. Several solutions could be obtained depending on the initial vorticity distribution, rendering it possible to transfer between two solutions of equal sign of the helical pitch. Further, contrary to the common conception, Okulov *et al.* [15] showed theoretically and numerically that vortex breakdown can occur even if there is no change in flow topology.

9. CONCLUSIONS

The helical parameters displayed a smooth, linear variation along the bump surface except for the estimate of the circulation, which was not accurate using this method. After passing the trailing edge of the bump, the trend deviated from the previous one and the helical vortex experienced an abrupt transition from one state to another without changing sign of the helical pitch. It has previously been shown both theoretically and computationally that this kind of transition is possible [14].

ACKNOWLEDGMENTS

The Danish Research Council, DSF, is acknowledged for their financial support of the present work under grant 2104-04-0020.

REFERENCES

[1] Adrian, R. J. (2007) Hairpin vortex organization in wall turbulence. *Physics of Fluids*, **19**, 041301.

[2] Görtler, H. (1955) Dreidimensionales zur Stabilitätstheorie laminarer Grenzschichten. *ZAMM*, **35**, 326.

[3] Taylor, H. D. (1947) The elimination of diffuser separation by vortex generators. Research Department Report No. R-4012-3, United Aircraft Corporation, East Hartford, Connecticut.

[4] Smith, F. T. (1994) Theoretical prediction and design for vortex generators in turbulent boundary layers. *Journal of Fluid Mechanics*, **270**, 91-131.

[5] Liu J., Piomelli, U. & Spalart, P. R. (1996) Interaction between a spatially growing turbulent boundary layer and embedded streamwise vortices. *Journal of Fluid Mechanics*, **326**, 151-179.

[6] You, D., Wang, M., Mittal, R. & Moin, P. (2006) Large-eddy simulations of longitudinal vortices embedded in a turbulent boundary layer. *AIAA Journal*, **44**, 3032-3039.

[7] Schubauer, G. B. & Spangenberg, W. G. (1960) Forced mixing in boundary layers. *Journal of Fluid Mechanics*, **8**, 10-32.

[8] Shabaka, I. M. M. A., Mehta, R. D. & Bradshaw, P. (1985) Longitudinal vortices imbedded in turbulent boundary layers. Part 1. Single vortex. *Journal of Fluid Mechanics*, **155**, 37-57.

[9] Godard, G. & Stanislas, M. (2006) Control of a decelerating boundary layer. Part 1: Optimization of passive vortex generators. *Aerospace Science and Technology*, **10**, 181-191.

[10] Velte, C. M., Hansen, M. O. L. & Cavar, D. (2008) Flow analysis of vortex generators on wing sections by stereoscopic particle image velocimetry measurements. *Environmental Research Letters*, **3**, 015006.

[11] Velte, C.M., Hansen, M.O.L. & Okulov, V.L. (2009) Helical structure of longitudinal vortices embedded in turbulent wall-bounded flow. *Journal of Fluid Mechanics*, **619**, 167-177.

[12] Zhang, X. (2000) Turbulence measurements of an inclined rectangular jet embedded in a turbulent boundary layer. *International Journal of Heat and Fluid Flow*, **21(3)**, 291-296.

[13] Schmidt, J. J. (1997) Experimental and numerical investigation of separated flows. *Ph.D. Thesis*, Department of Mechnical Engineering, Tehcnical University of Denmark.

[14] Martemianov, S. & Okulov, V. L. (2004) On heat transfer enhancement in swirl pipe flows. *International Journal of Heat and Mass Transfer*, **47**, 2379-2393.

[15] Okulov, V. L., Sørensen, J. N. & Voigt, L. K. (2005) Vortex scenario and bubble generation in a cylindrical cavity with rotating top and bottom. *European Journal of Mechanics B/Fluids*, **24**, 137-148.